PHYSICAL REVIEW B **90**, 205208 (2014)

Voltage-controlled oxide barriers in organic/hybrid spin valves based on tunneling anisotropic magnetoresistance

M. Grünewald, N. Homonnay, J. Kleinlein, and G. Schmidt*

Institute of Physics, Martin-Luther-Universität Halle-Wittenberg, Von-Danckelmann-Platz 3, D-06120 Halle, Germany

(Received 14 April 2014; revised manuscript received 21 October 2014; published 14 November 2014)

Resistive switching, i.e., the remanent (reversible) change of a device's resistance, is a widely investigated phenomenon as it holds the prospect for realizing high density memory devices. Resistive switching has also been observed in organic semiconductors; however, a clear understanding of the underlying physics could not yet be obtained. Possible options are for example interface effects at the electrodes or the formation and destruction of filaments. Here we present resistive switching in an organic spin valve based on tunneling anisotropic magnetoresistance. Similar to experiments in conventional spin-valve devices with two ferromagnetic electrodes we observe a modulation of the magnetoresistance by the electrical switching. However, as the magnetoresistance effect's origin is unambiguously clear, which is not always the case for effects in conventional structures, it can be exploited to prove that a tunnel barrier exists at the interface between the ferromagnetic oxide electrode and the organic semiconductor. Furthermore our experiments reveal that this barrier is reversibly modified during the switching, which causes both the change in magnetoresistance and total device resistance. Quantitative analysis indicates that the barrier is situated in the oxide layer. A phenomenological model provides a full description of the microscopic processes involved in the resistive switching.

DOI: 10.1103/PhysRevB.90.205208 PACS number(s): 81.05.Fb, 75.47.Lx, 73.40.−c

I. INTRODUCTION

Resistive switching (RS) was first demonstrated in 1962 [1]. It gained technological interest in the 1990s and then became a wider research area when the first memristor devices [2] were realized. RS is used as a keyword for phenomena that comprise the nonvolatile and often reversible modification of a device's electrical resistance R, typically initiated by the application of a voltage or current pulse. Frequently, RS is observed in vertical metal-insulator-metal structures where the insulating layer is an oxide [1,3–12]. A lot of models explaining the RS phenomenon for a specific material system have been proposed [4–14], some of them elucidating the importance of oxygen vacancies (V_Os) in the oxide layer [6–10,12] that can be formed/removed, for instance, by electrochemical redox reactions [8,10,12,15].

In recent years, RS also has been demonstrated in devices comprising an organic semiconductor layer instead of an inorganic insulator [16–25]. Although most of these experiments were undertaken for structures with nonmagnetic electrodes, also a few results exist from organic spin valves, i.e., devices with ferromagnetic contacts [20,23,25]. In a spin valve the device resistance can be switched between two well defined states by applying a magnetic field, which is referred to as spin-valve behavior or magnetoresistance. Hueso *et al.* [20] were the first to show a device which exhibits both effects, RS and magnetoresistance, thus giving prospect to multifunctional applications [25]. However, in most cases the origin of the magnetoresistance in organic spin valves is unclear [26,27] because it is difficult to say whether the device resistance originates from charge transport through the semiconductor, tunneling, or both. In addition, the interfaces between the organic semiconductor and the electrodes often include tunnel barriers which can contribute a substantial part of the device resistance [28,29]. Understanding of the physics behind the spin-valve functionality and its interplay with RS is thus still rather poor and therefore requires additional experiments.

Tunneling anisotropic magnetoresistance (TAMR) [30] is another magnetoresistance effect that can be observed in spin-valve-like devices with only one ferromagnetic electrode. It has been shown that TAMR can mimic spin-valve behavior in inorganic [30–33] and likewise in organic devices [34]. In the latter the ferromagnetic electrode usually is a $La_{0.7}Sr_{0.3}MnO_3$ (LSMO) layer. In contrast to the magnetoresistance in conventional organic spin valves, results obtained in organic TAMR devices can be interpreted in a very straightforward manner. If TAMR is observed its origin is unambiguously tunneling into or from the crystalline ferromagnetic electrode.

We have studied RS and TAMR in LSMO-organic semiconductor-Cu structures where we observe a clear interaction between both effects. In these structures TAMR is used for probing the tunnel barrier between the LSMO electrode and the organic semiconductor. Our key result is a decisive proof that this injection barrier is modified during the RS measurements, which has been analyzed qualitatively and, to a certain extent, quantitatively by I/V characterization. All experimental results are condensed into a model that is based on the formation, motion, and removal of pairs of a V_O and an interstitial oxygen ion at the LSMO-organic-semiconductor interface.

II. EXPERIMENTAL PROCEDURES

A. Sample fabrication

The TAMR devices under investigation are standard vertical transport structures. One sample consists of 8 single devices (active area $200\times150\ \mu m^2$) that share a common LSMO bottom contact. The sample fabrication was performed in a UHV-cluster system allowing for the use of different deposition methods without breaking the vacuum (pulsed laser

*Corresponding author: georg.schmidt@physik.uni-halle.de

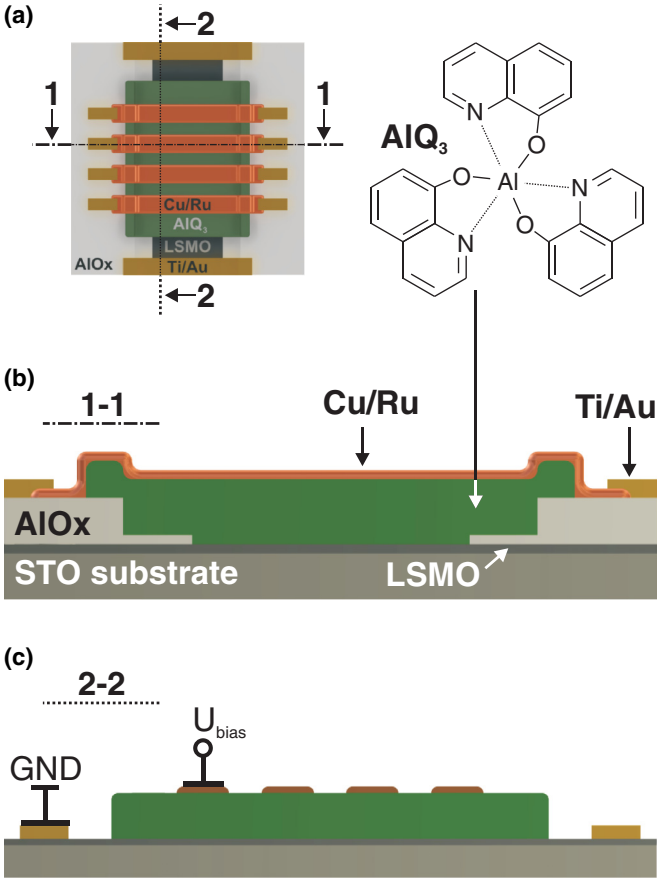

FIG. 1. (Color online) Schematic top view on a sample with 4 TAMR structures, cross section of a single device, cross section of the sample, and molecular structure of the organic semiconductor tris-(8-hydroxyquinoline)aluminium (AlQ_3).

deposition, electron beam evaporation of metals and insulators, sputtering of metals, organic molecular beam deposition). Furthermore a system for the *in situ* exchange of solid shadow masks (made of 100 μm thick stainless steel) is attached to the UHV cluster.

A schematic representation of a sample (top view and cross sections) is shown in Fig. 1. The samples are fabricated on strontium titanate (001) substrates on which first a film of LSMO (thickness 20 nm) is deposited by pulsed laser deposition. Subsequently the sample is prepared for the shadow mask deposition system and all following steps are performed *in situ*. The LSMO layer is patterned indirectly by depositing two layers of alumina (AlOx, electron beam evaporation) leaving uncovered a stripe of 200 μm$\times$ 5 mm. This stripe serves as common bottom contact for all devices. The first alumina layer defines the dimension of this stripe and is rather thin (thickness 15 nm) in order to avoid shadow effects during the deposition of the other materials. The second one, deposited on top of the first, is thicker (thickness 100 nm) to ensure good insulating behavior at high voltages and mechanical stability during later ultrasonic bonding. The following organic semiconductor is thermally evaporated (organic molecular beam deposition) from a Knudsen cell. This layer is made of tris-(8-hydroxyquinoline)aluminium [AlQ_3, thickness 60 nm, molecular structure shown in Fig. 1(a)], one of the standard materials in organic spintronics research [20,26,27,35–38]. During the AlQ_3 deposition a shadow mask with a large rectangular window is used. Subsequently dc sputtering is applied to deposit the Cu top contact (thickness 20 nm) and the Ru capping layer (thickness 10 nm) through a shadow mask with 8 stripe-shaped openings (width 150 μm) defining the separate devices. The last step is the evaporation of Ti/Au contact pads by electron beam evaporation. With this process clean and reproducible interfaces are achieved. Furthermore it is important to note that whenever electron beam evaporation is used the sensitive device area is covered by the respective shadow mask in order to avoid side effects caused by eventual x-ray or electron emission from the evaporator [39].

B. Transport measurements

All transport experiments, the investigation of TAMR and RS, were conducted at 4.2 K in a ^{4}He bath cryostate with a 3D vector magnet with which magnetic fields up to 400 mT can be applied in any direction in space. The device resistance was measured using a current amplifier with variable gain and an Agilent 34420A nanovolt/micro-ohm meter. The bias voltage and voltage pulses are supplied by a self-built high-precision digital-to-analog converter.

In the RS measurements short voltage pulses of increasing/decreasing height (U_{pulse}, pulse length $t_{\text{pulse}} = 50$ ms) are applied to the device where U is applied to the top contact and the LSMO electrode represents electric ground [see Fig. 1(c)]. In between the pulses the device resistance is measured at a low bias voltage of $U_{\text{bias}} = 1$ mV. The choice of this technique is motivated by a substantial simplification of the results' interpretation. As the device resistance is measured at a fixed U_{bias} a potential nonlinearity of the I/V curve does not appear in the RS trace and any change of the device resistance is reflected in the measurement data immediately and unambiguously. Thus, this method yields clear results and an enhanced controllability of the experiment.

III. RESULTS AND DISCUSSION

A. Resistive switching behavior

The RS observed in our devices is induced by applying voltage pulses (U_{pulse}) as described above. We quantify RS by plotting the device resistance over U_{pulse}. U_{pulse} is applied in a sequence of steps in a range between $\pm$10 V whereby the maximum range used for a specific measurement is device dependent. The exemplary result shown in Fig. 2(a) is obtained by using pulse heights in the $\sim\pm$2.6 V regime. The initial state has the minimum device resistance (base resistance state, BRS, $R_{\text{BRS}} \approx 1.6$ kΩ). When a positive voltage pulse is applied the device resistance does not change to a measurable extent [for the sake of clarity, parts of the trace with constant device resistance are omitted in Fig. 2(a)]. At high negative U_{pulse} (~-2.55 V, blue/dark gray curve), however, a sharp increase of the device resistance resulting in the low resistance state (LRS, R_{LRS}) is observed. R_{LRS} depends on the magnitude of the minimum U_{pulse} and can be as high as $R_{\text{LRS}} \approx 5$ kΩ for the present device. Starting from the LRS, subsequently voltage pulses with opposite polarity are applied. For the case of bipolar switching [3] one would expect a constant

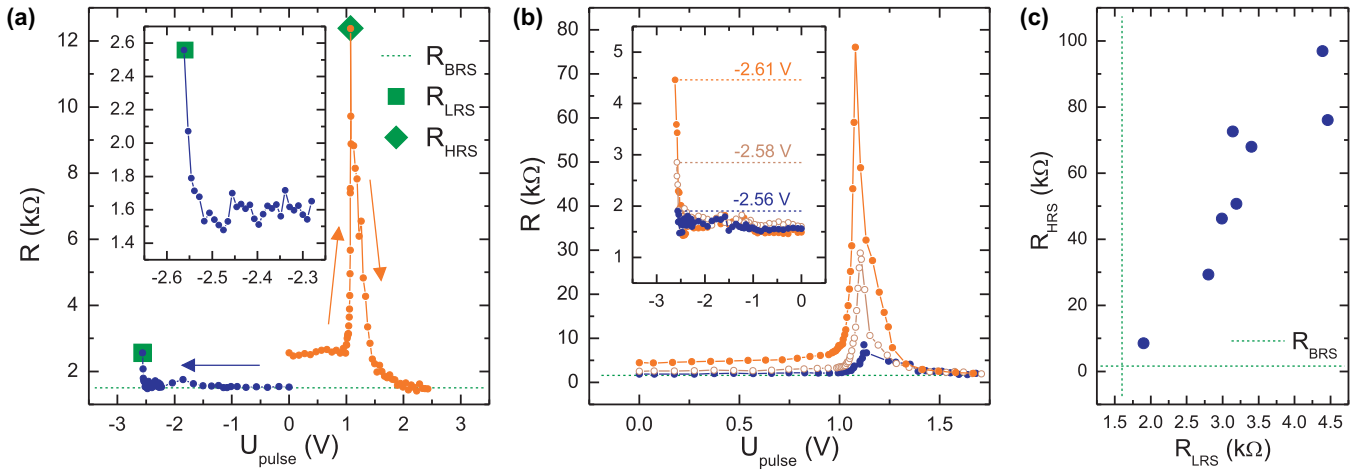

FIG. 2. (Color online) Basic features of the resistive switching in organic TAMR devices. (a) A full RS hysteresis showing the three resistive states mentioned in the text: BRS is the base resistance state (minimum device resistance), LRS the low resistance state reached by applying sufficiently high negative voltage pulses (as shown in the inset), and HRS the high resistance state, which is accessible from the LRS by applying intermediate U_{pulse} in the positive regime. Higher positive voltage pulses result in a switching to the BRS again. Sweeps from maximum positive/negative U_{pulse} to $U_{\text{pulse}} = 0$ V yield a constant device resistance and therefore are omitted. (b) The height of the maximum in the HRS depends on the previously prepared LRS state as shown for three different cycles. Different LRSs can be achieved by stopping the sweep in the negative U_{pulse} regime at different pulse heights. (c) The relation between R_{HRS} and R_{LRS} is linear.

device resistance until at a certain threshold the device is set back to the BRS. Although at relatively high positive U_{pulse} indeed the BRS is restored, intermediate positive pulses yield a remarkable result, namely a further increase in device resistance and a sharp maximum at $U_{\text{pulse}} \approx +1.1$ V (high resistance state, HRS, R_{HRS}). Hence, in contrast to conventional bipolar switching the RS signal in our devices comprises at least the three distinguished states marked in Fig. 2(a).

As shown in Fig. 2(b) R_{HRS} is correlated with the previously prepared LRS. Apparently this correlation is linear as the summary of several RS sweeps with different LRSs and consequently different HRSs in Fig. 2(c) reveals.

B. TAMR analysis

TAMR originates from spin-orbit coupling in a ferromagnetic electrode consisting of a material with magnetocrystalline anisotropy [30]. When in such a material the magnetization vector is rotated with respect to the lattice, the spin-orbit coupling causes a change in the k dependence of the density of states. If this electrode is part of a tunnel junction hereby the tunneling probability and thus the tunneling resistance is changed. For a material with a biaxial anisotropy and a symmetry breaking between the two easy axes, which applies to the LSMO used in our experiment [40], TAMR can mimic spin-valve behavior [30]. For such a configuration any magnetic field (B_{ip}) sweep in the plane along any direction φ off the easy axes results in a magnetization reversal in two 90° steps [Fig. 3(a)] [41]. In consequence, the resulting magnetoresistance trace comprises two different tunneling resistance states ($R_{H/L}$) and bears resemblance to a typical spin-valve signal [Fig. 3(b)]. Already in a previous work TAMR has been demonstrated for organic devices based on an LSMO electrode [34]. Also in the present structures we obviously observe TAMR as revealed by the typical magnetoresistance result recorded at $T = 4.2$ K [device in the BRS, Fig. 3(c)]. In order to unambiguously identify TAMR the measurement was repeated for $\varphi = 0°$–$180°$ yielding the signals summarized in Fig. 3(d). These data contain all typical features of TAMR, namely an angle-dependent sign change of the effect, the shift of the switching fields (named $B_{c,1/2}$), and the absence of the spin-valve signature for distinguished φ. Further confirmation for TAMR comes from superconducting quantum interference device (SQUID) analysis of the structures (bottom panels of Fig. 4) which is used to investigate the LSMO electrode's magnetization reversal when B_{ip} is applied off the easy axes (denoted by φ_{off} in Fig. 4). The hysteresis loops unmistakably show that the magnetization is reversed in two steps. A comparison with the magnetoresistance traces in the top panels of Fig. 4 indicates that these two steps occur at the same fields as the magnetoresistive switching between the two resistance states.

The presence of TAMR clearly shows that part of the device resistance stems from a tunnel barrier which also is reflected in the nonlinear I/V curves [see Fig. 14(a) in Appendix B]. As TAMR can only occur when charge carriers are extracted from or injected into the LSMO electrode, the effect must be originating from the interface between the LSMO and the AlQ_3 layer. As already mentioned before, charge injection into an organic semiconductor via a tunnel barrier is a very likely scenario [28,29]. Control experiments in structures where the AlQ_3 layer is omitted and where no effect, neither TAMR nor RS, is observed underline the governing role of this specific interface.

C. Analysis of the resistive switching effect

We have used two methods of analysis in order to gain insight into the underlying physics of the RS behavior. The first straightforward method is to check whether the TAMR response changes when the device resistance is set to different

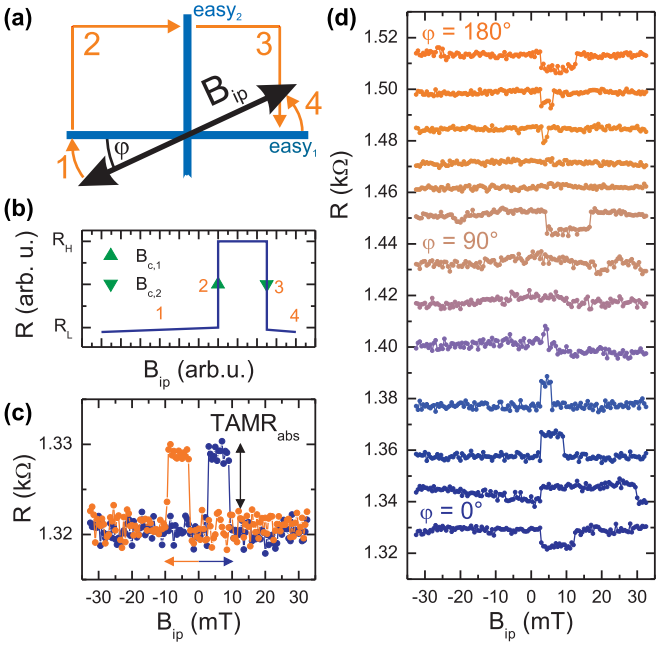

FIG. 3. (Color online) Summary of TAMR results obtained from magnetotransport studies in an LSMO-AlO_3-Cu device. (a), (b) Schematic representation of the double step magnetization reversal of the LSMO electrode and the resulting magnetoresistance curve. Characteristic switching steps are denoted by numbers. (c) Single magnetoresistance measurement for one in-plane direction φ exhibiting TAMR. The device resistance clearly is switched between two distinct resistance states (R_L and R_H) that can be attributed to the LSMO layer being magnetized along one of the two respective easy axes. The magnetoresistance ratio $\mathrm{TAMR_{abs}}/R_L$ is ∼0.75%. (d) Results of several magnetoresistance measurements with different φ (single curves are offset by ∼16 Ω for the sake of clarity) reveal all typical features of TAMR. A clear shifting of the switching fields $B_{c,1/2}$ as well as a change of the effect's sign is observed when φ is changed. For distinguished directions the effect vanishes identifying those as the easy axes of the LSMO electrode.

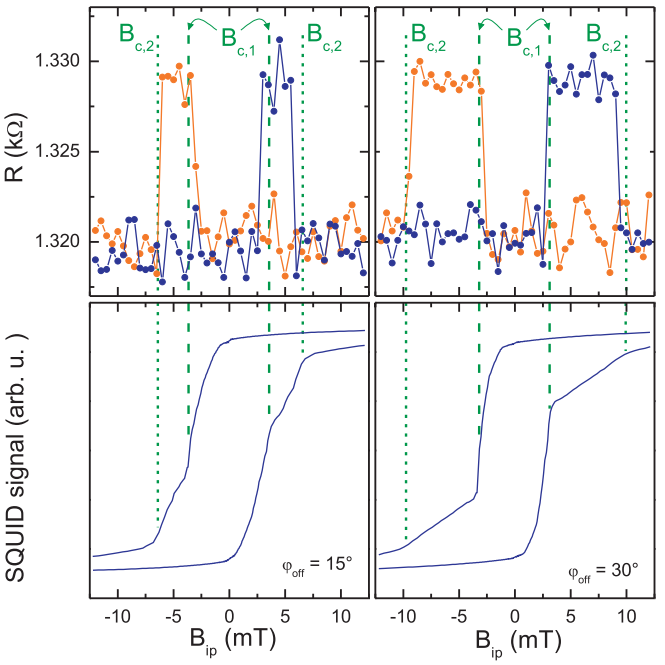

FIG. 4. (Color online) Comparison of single TAMR traces with SQUID measurements done by applying the magnetic field along identical orientations (denoted by the offset from the easy axis φ_{off}), respectively, evidencing that the LSMO's magnetization is reversed in two steps. The $B_{c,1/2}$ in SQUID and magnetoresistance measurement coincide. All measurements at $T = 4.2$ K and $U_{\mathrm{bias}} = 5$ mV.

values. As this change is indeed observed, qualitative and quantitative information concerning a potential modification of the tunnel barrier is obtained by the second procedure, an evaluation of I/V curves. A number of HRSs with R_{HRS} in the range of 5–120 kΩ have been prepared and investigated employing standard magnetotransport and I/V characterization. After the investigation of a unique HRS the BRS is reestablished and the next HRS is set.

In the first place, the TAMR amplitude is now analyzed as absolute resistance difference $\mathrm{TAMR_{abs}}$ as indicated in Fig. 3(c). In Fig. 5(a) $\mathrm{TAMR_{abs}}$ is plotted against the respective R_{HRS}. Obviously, there is a clear correlation between $\mathrm{TAMR_{abs}}$ and R_{HRS} that appears as a linear increase of $\mathrm{TAMR_{abs}}$ for $R_{\mathrm{HRS}} \lesssim 85$ kΩ, while for higher R_{HRS} the absolute effect size apparently saturates. As the relative TAMR ratio [$\mathrm{TAMR_{abs}}/R_L$, inset of Fig. 5(a)] is also raised significantly, a pure scaling of TAMR proportional to a scaled device resistance can be excluded. Instead, we assume that the total resistance is composed of the tunnel barrier and a series resistance. During the RS the resistance of the tunnel barrier increases and the TAMR scales with this increase, thus enhancing the ratio $\mathrm{TAMR_{abs}}/R_L$. This can be explained by modifications of either the LSMO electrode's density of states or the tunnel barrier itself. Alternative theoretical approaches to TAMR amplitudes as high as they are observed here ($\mathrm{TAMR_{rel}} \approx 20\%$ as shown in Fig. 5(b) is more than the sixfold of the typical values reported so far [30–33]) can be found in the work of Gould *et al.* [30]. However, these models are omitted here because they usually comprise fundamental improvements of the buried injection interface that are not consistent with a voltage-induced modification.

Thus, the results in Fig. 5(a) indicate a modification of the tunnel barrier. For the following discussion and evaluation of the data it is now assumed that this injection barrier is composed of two components which are the actual interface injection barrier at the LSMO-AlO_3 contact (contact barrier) and an adjacent barrier at the LSMO layer's surface. All results we have shown so far clearly reveal that already at small bias voltages a measurable current is driven through our devices and hence the interface injection barrier must be rather low. This likewise is reported in various other studies investigating organic spin valves [20,26,27,35,37] and can be explained by the formation of either hybridization-induced states [42] or a dipole at the interface LSMO-AlO_3 [29,43]. Furthermore this contact barrier can be regarded as stable whereas the tunnel barrier located at the LSMO layer's surface is variable as will be demonstrated by the following analysis of I/V curves collected for different HRSs.

In order to derive barrier parameters, e.g., barrier width d_{barrier} and energetic height Φ_0, from I/V curves it is necessary that the current flow be homogeneous over the whole barrier.

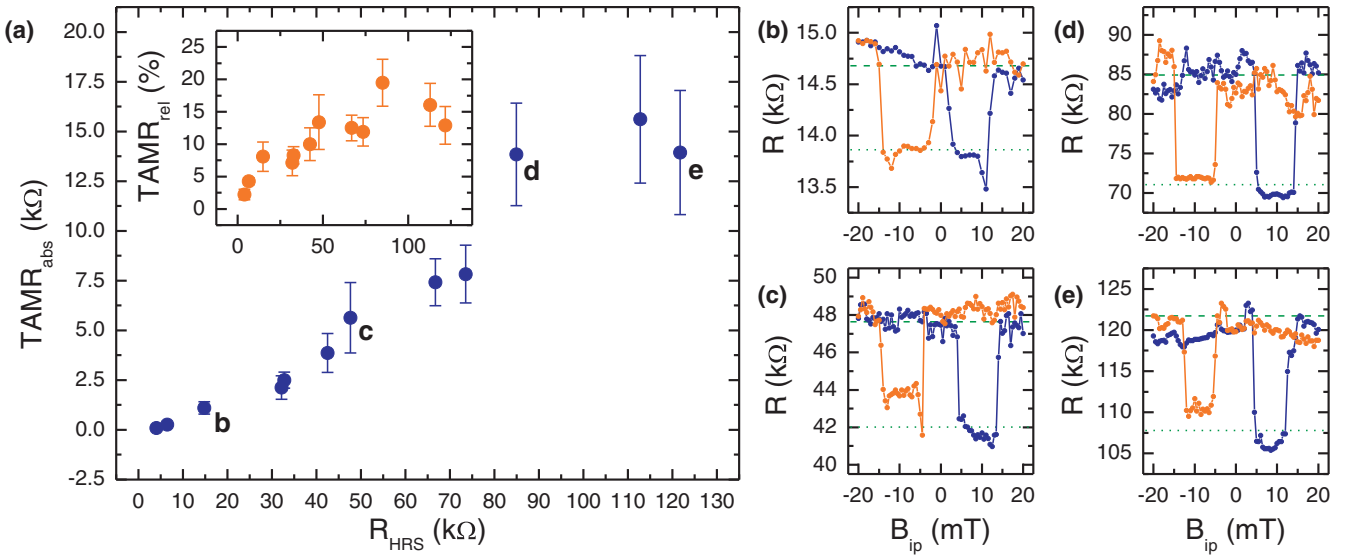

FIG. 5. (Color online) Magnetotransport measurements are undertaken for different HRSs of the same device. (a) The results unambiguously reveal a clear interaction between the RS and TAMR effect. The latter is enhanced with increasing R_{HRS} suggesting a modification of the injection barrier. (b)–(e) Single MR traces show the reproducibility of the spin-valve-like signal caused by TAMR at different R_{HRS}. The dashed and dotted lines indicate the average high and low resistance used for the calculation of the error in a single measurement. The error bars in (a) are derived from averaging results of several single MR measurements for each R_{HRS}.

This is only the case if the resistance of the materials on both sides of the barrier is small enough compared to the barrier resistance. Although the in-plane resistance of the LSMO is experimentally determined to be $\ll 100\ \Omega$ and hence much smaller than the total device resistance, estimating the current distribution can prove difficult. We have thus performed finite element simulations using our material parameters and the measured device resistance which show that the assumption of two equipotential planes on both sides of the barrier is justified and indicate that the density of the tunneling current is constant over the whole device area (see also Appendix A). It is thus allowed to treat the device as one-dimensional as illustrated in Fig. 6(a) and to calculate the current density j by dividing the current by the active device area.

Subsequently the differential tunnel conductance dj/dU_{bias} can be derived from j for the evaluation of the I/V characteristics. This data is then analyzed using the Simmons model [44] which can be applied when the bias voltage is small compared to the barrier height (for larger bias other models like Fowler Nordheim tunneling [45] must be employed). In our analysis we only fit data below ± 5 mV [see also Fig. 14(b) in Appendix B] yielding a perfect parabolic fit. At the same time the very low bias voltages investigated allow us to average the height of the barrier, i.e., to treat the barrier as basically rectangular [44], and to assume that any tilt of the barrier due to the bias is small compared to the barrier height Φ_0, both other important prerequisites for the Simmons fit's evaluation outlined in detail in Appendix B. This procedure allows for the determination of d_{barrier} and Φ_0 from a parabolic fit to dj/dU_{bias} [Eqs. (B2) and (B3) in Appendix B]. For simplification we furthermore assume that the barrier resistance dominates the device resistance and contributions from other parts of the device can be neglected. This is justified by the observed rise in TAMR with increasing device resistance.

First, I/V curves recorded together with the TAMR measurements summarized in Fig. 5 are investigated yielding the results shown in Figs. 6(b) and 6(c). In order to get a clearer picture of the effect we plot the respective difference between d_{barrier} and Φ_0 in the high resistance state and their initial values

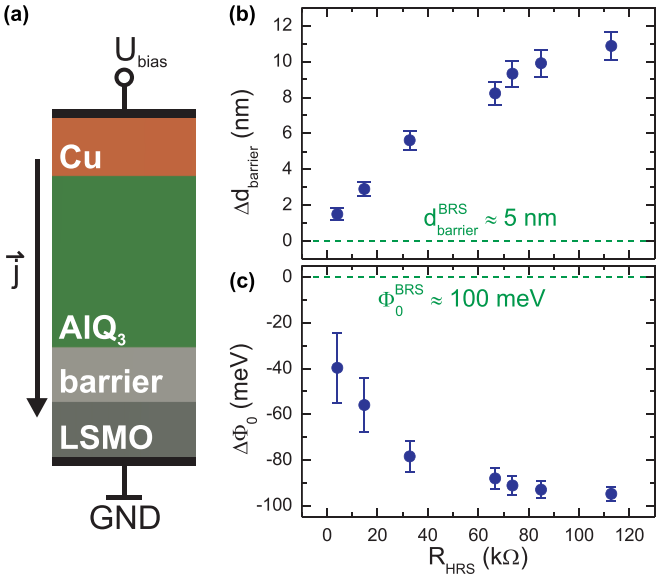

FIG. 6. (Color online) Experimental evidence for the injection barrier's modification due to the application of voltage pulses. (a) The analysis of the tunnel barrier at the LSMO-AlQ_3 interface is undertaken assuming this one-dimensional representation of the device which is supported by simulation results. (b), (c) Quantitative analysis of the barrier modification obtained from Simmons fits to I/V curves taken at different HRSs. The barrier parameters are displayed as difference to the respective values obtained for the BRS. The error bars are calculated from the fit parameters.

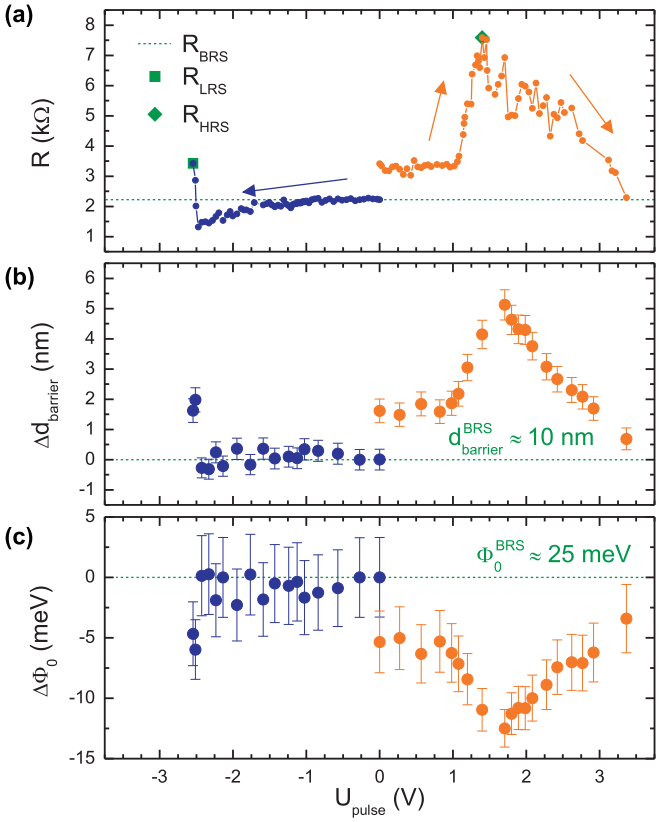

FIG. 7. (Color online) Quantitative analysis of the barrier modification [barrier thickness in (b) and barrier height in (c)] obtained from Simmons fits to I/V curves recorded during the RS loop shown in (a).

in the base resistance state. These data show that the tunnel barrier at the LSMO-AlQ_3 interface gets thicker and lower with increasing R_{HRS}.

The same analysis is performed for I/V characteristics acquired during a RS loop in another device. The determined $\Delta d_{barrier}$ and $\Delta\Phi_0$ are shown in Fig. 7 together with the corresponding RS trace. The results are consistent with those discussed above. Whenever an increase of the device resistance is observed, $d_{barrier}$ is enhanced and Φ_0 is reduced and vice versa. Furthermore, it gets clear that after the cycle, i.e., when the BRS is restored at high positive U_{pulse}, the barrier is completely reset to its initial state.

Further characteristic features of the RS effect can be unveiled by performing RS minor loops. The minor loops are taken using pulse voltages between those necessary to establish the LRS or the HRS (U_{LRS}, U_{HRS}). They are reproducible when repeated using the same sweep parameters for U_{pulse}. Starting from the LRS [blue/dark gray line in Fig. 8(a)], a minor loop (green/light gray line) comprises a U_{pulse} sweep from a negative start value to a positive U_{stop} (which is below U_{HRS}) and back. U_{stop} is chosen such that the sweep direction is reversed at an intermediate resistive state (IRS, R_{IRS}) on the rising edge between the LRS and HRS. Hereby, a closed and nearly symmetric hysteresis loop (height $\Delta R_{ML} = R_{IRS} - R_{LRS}$) is obtained.

On the basis of the same LRS, minor loops with different height and width can be run by varying U_{stop} as exemplary shown for five values of U_{stop} in Fig. 8(b). Evidently, the negative U_{pulse} required for resetting the LRS roughly corresponds to $-U_{stop}$. When the LRS is reached again, a further decrease of U_{pulse} yields no further change in device resistance until U_{LRS} is surpassed. It should be pointed out here that this minor-loop effect can be described as RS in the sense of the commonly known bipolar switching between two resistive states.

For RS minor loops the barrier parameters' dynamics also are characterized by the analysis of I/V responses taken during a minor-loop measurement similarly as shown in Fig. 7 for a full RS hysteresis. The minor loop under investigation can be found in Fig. 8(c). The barrier parameters are displayed as differences to the respective values obtained for the underlying LRS in Figs. 8(d) and 8(e). Besides the already discussed behavior of increasing (decreasing) barrier thickness (height) with increasing device resistance these results reveal that again after a full and closed minor loop the initial barrier obviously is restored.

Furthermore, we have investigated the stability of the resistive states with respect to a temperature increase. The state under investigation is prepared at $T = 4.2$ K. T is then increased to $T_{heat} = 290$ K. After 10 minutes at T_{heat} the sample is cooled to 4.2 K again. I/V curves are recorded at 4.2 K before and after the heating-cooling cycle. In a first experiment, this procedure is performed for three distinguished states, namely the BRS, the LRS, and one IRS (with $\Delta R_{ML} \approx 1$ kΩ). These states are marked on the corresponding RS trace in Fig. 9(a). From a comparison of the two I/V curves recorded for each state we can conclude that the BRS and LRS are not influenced by the interim temperature change (Fig. 15 in Appendix C). However, in the case of the IRS a decrease of the device resistance is measured after the heating-cooling cycle. ΔR_{ML} is reduced by ∼55% as illustrated by the green/light gray arrow in Fig. 9(a). This thermally induced change of the device resistance, which is referred to as ΔR_T hereafter, again is due to a decrease of $d_{barrier}$ and an increase of Φ_0. Hence, one can conclude here that the barrier's modifications initiated by U_{pulse} during the transition LRS → IRS can partially be reversed by thermal activation, which is not the case for the change BRS → LRS. Similar observations of such a resistive state's relaxation and its temperature dependence can be found in the literature for RS in other perovskites as well, for example for $Pr_{0.7}Ca_{0.7}MnO_3$ [6].

If after the temperature cycle the positive U_{pulse} that was used for the preparation of the IRS is again applied at $T = 4.2$ K the initial IRS is regained. If, however, the minor loop that has been interrupted for the heating-cooling procedure is continued from the reduced IRS by a suitable sweep towards negative U_{pulse} the original LRS is restored. As a consequence of this, ΔR_T can be analyzed for different T_{heat} but for the same minor-loop parameters, i.e., the same LRS and IRS, using the following protocol. Having set the LRS, the IRS is prepared and a heating-cooling cycle including the aforementioned I/V characterization is performed. Finally, the minor loop is closed, i.e., the LRS is restored and serves as starting point of the next cycle with a different T_{heat}. The same sweep parameters corresponding to $R_{LRS} \approx 0.55$ kΩ and $R_{IRS} \approx 1.55$ kΩ are used for all $T_{heat} = 20$–290 K.

Figure 9(b) shows the results of such an experiment for ΔR_T and the modifications of the barrier parameters $\Delta d_{barrier}$

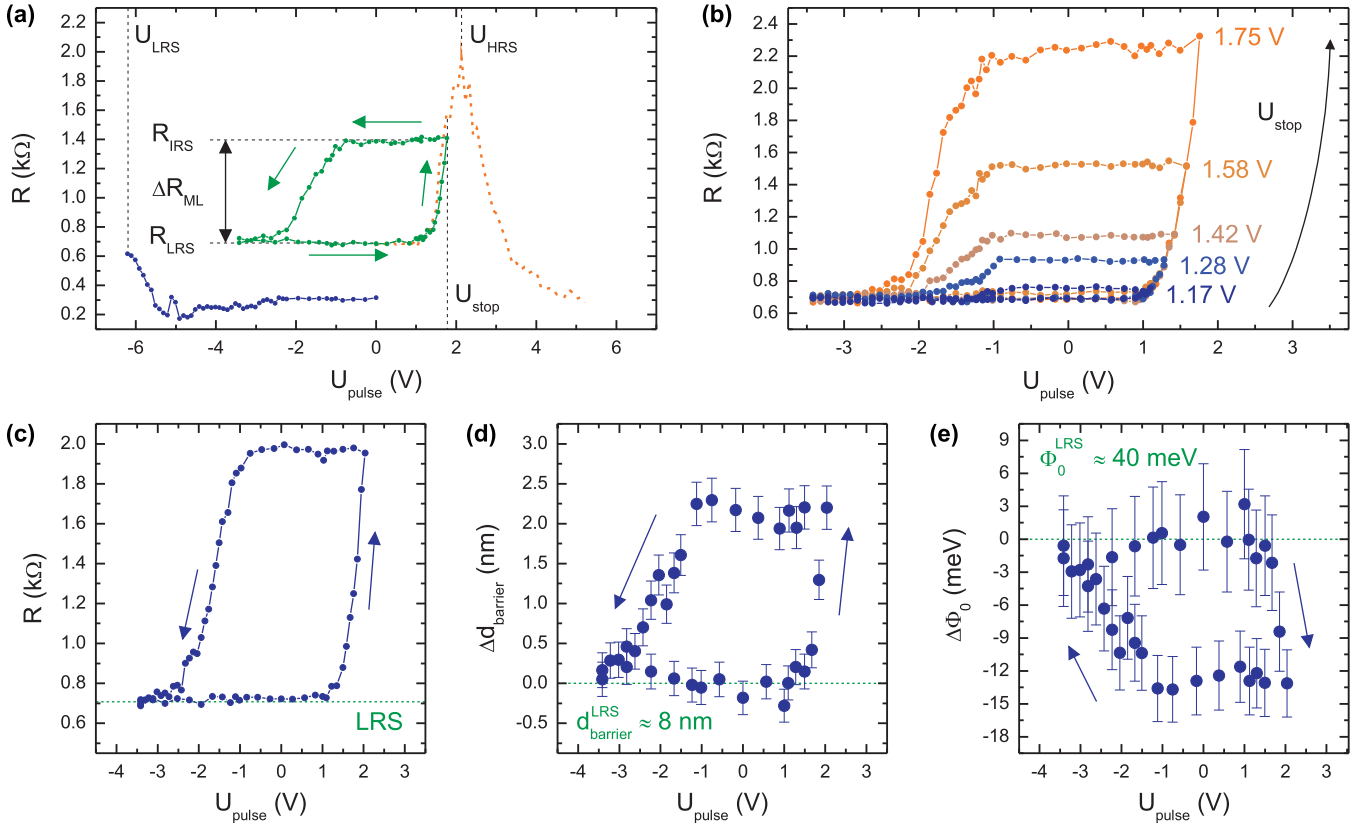

FIG. 8. (Color online) Analysis of the RS behavior using minor loops. (a) Minor loop (green/light gray line) after preparation of the LRS (blue/dark gray line). The U_{pulse}-sweep direction is reversed on the rising edge between the LRS and HRS at U_{stop}. The dashed orange trace is recorded after the minor-loop measurement. (b) Minor loops acquired with different U_{stop} exhibit different heights ΔR_{ML} and widths. Sweeping back from any IRS always yields the same LRS. (c)–(e) Quantitative analysis of the barrier modification [barrier thickness in (d) and barrier height in (e)] obtained from Simmons fits to I/V curves recorded during the minor loop shown in (c).

and $\Delta\Phi_0$. The data are represented as relative values with respect to those present before the heating-cooling cycle. Evidently, for $T_{\text{heat}} < 100$ K we do not observe a substantial change of the IRS, whereas for higher T_{heat} an increase of $|\Delta R_T|$ along with corresponding changes in d_{barrier} and Φ_0 appears. The maximum $\Delta R_T \approx -0.55 \times \Delta R_{\text{ML}}$ is observed for $T_{\text{heat}} = 290$ K.

As a final remark, it should be mentioned that, from device to device, variations of the devices' resistance of approximately one order of magnitude are measured directly after sample fabrication. This suggests that different interfacial tunnel barriers may be present in the first place. Hence, it is very likely that likewise the specific features of a device with respect to the observed RS dynamics are determined by local characteristics of the interface LSMO-AlQ_3.

IV. PHENOMENOLOGICAL MODEL

A. Description

We propose a model to describe the observed RS behavior and its interaction with the TAMR effect that is based, similarly to other models in the literature [4,6–10,12], on the influence of the LSMO's local stoichiometry on its conductivity. Considering oxygen ions that are removed from lattice sites onto interstitial sites and V_Os as species governing the RS all features of the effect can readily be explained as will be discussed below.

Effects originating from the AlQ_3 layer [19–23,25] cannot be deemed promising candidates here for the following reasons. RS in AlQ_3-based structures with nonmagnetic contacts either requires an Al/AlQ_3 interface [19,21] or a modification of the organic layer by adding MoO_3 nanoparticles or nanoclusters during fabrication [22], both preconditions which are not fulfilled in our devices. The models proposed for organic spin valves comprising the interface LSMO-AlQ_3 involve the formation and charging of trapping domains [14,23] or the formation and rupture of highly conducting filaments [20,25] in the AlQ_3 layer, which might explain a bipolar switching but not the observed increase in TAMR which clearly localizes the effect at the LSMO surface. Furthermore an increase of the device resistance for both polarities of the applied voltage pulse allegedly cannot be integrated into these scenarios in a straightforward and intuitive manner.

Instead, as already mentioned, a plausible and equally fundamental explanation can be derived from the experimental results assuming the origin of the RS in the LSMO electrode. Changing the stoichiometry of perovskites like LSMO with respect to the oxygen content by only a few percent can cause substantial modifications of the material, e.g., with respect to its structure, magnetization, and/or conductivity [46–49]. Usually, the oxygen content, and hereby the V_O concentration,

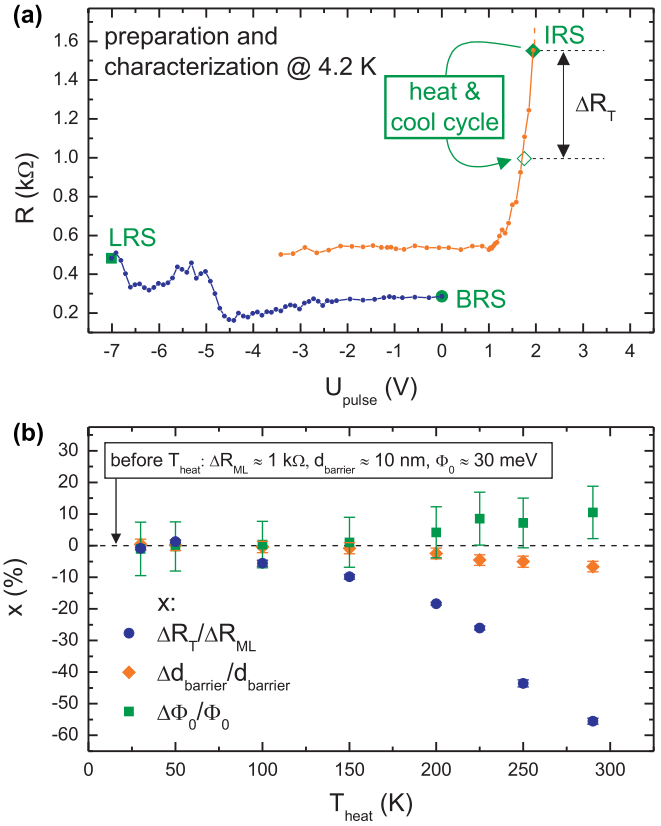

FIG. 9. (Color online) Analysis of the RS behavior employing heating-cooling cycles. (a) Summary of the experiment comprising an interim temperature change (heating-cooling cycle) for three distinguished resistive states (BRS, LRS, and IRS). Only the IRS is substantially modified which is established as a reduction of ΔR_{ML} by ΔR_T. (b) The effect of a temperature increase is investigated for different temperature set points T_{heat}. I/V characterization and Simmons fits are employed to analyze the tunnel barrier. The difference of the respective values obtained before and after the heating-cooling cycle are plotted as relative values (error bars: standard deviation for ΔR_T, calculated from fit parameters for d_{barrier} and Φ_0). A substantial modification is observed for $T_{\mathrm{heat}} \gtrsim 100$ K only.

is tuned either during layer growth [46–48] or afterwards for example by annealing [49]. Furthermore, it is confirmed that V_Os can be created/removed by electrochemical redox reactions in perovskites [4,8]. Recently, it has been clearly demonstrated that reactions altering the V_O content of an oxide can also be initiated by strong electric fields [15].

In the following discussion the RS, which obviously is more complex than common bipolar switching, is treated as consisting of two separate components. They can be distinguished by temperature stability of the resistive states that are involved in the respective component. Thus, the first part comprises the transitions BRS → LRS and HRS → BRS at high $|U_{\mathrm{pulse}}|$ which is stable upon increasing temperature. It is referred to as major loop hereafter [blue/dark gray curves in Fig. 10(a)]. The second feature is the aforementioned minor loop [orange/light gray curve in Fig. 10(a)], i.e., the transitions LRS → IRS/HRS and back, for which significant modifications are observed at elevated temperatures.

As stated above, the minor loop is not observed without prior preparation of the LRS. This, on one side, allows us to consider the major-loop switchings as processes that enable/disable the minor-loop functionality. On the other side, this fact suggests that some link between the two components has to be taken into account. This link is provided by the key assumption that only pairs of one V_O and one interstitial oxygen ion (O_{is}^{2-}), respectively, are involved in the microscopic mechanisms behind the RS effect. Both particles can be added and removed close to the LSMO-AlQ_3 interface (major loop) and equally be moved inside the LSMO (minor loop) as we will outline below. The oxygen deficiency in the LSMO adds a variable tunnel barrier to the initial (nonvarying) injection barrier at the LSMO-AlQ_3 interface.

In the following we describe the full process of barrier formation, modification, and removal. For the sake of clarity the graphical representation uses the simplified picture of a rectangular barrier. Although this is a coarse approximation it is sufficient for the understanding of the effect and for the basic quantitative consideration as is also done in the Simmons model [44]. The details of the shape of the barrier can only be obtained by determining the exact distribution of V_Os in the LSMO layer in the different states which is not accessible in our experiments.

To simplify the graphical representation we assume that in the BRS the LSMO is entirely intact; i.e., R_{BRS} originates from the contact barrier only [Fig. 10(b)]. The presence of a thin barrier in the BRS is confirmed by the occurrence of TAMR. For the major loop switching BRS → LRS an increase of d_{barrier} is revealed by the I/V analysis. In the proposed scenario, this transition therefore is equivalent to the creation of V_Os at the interface LSMO-AlQ_3, which may be caused by the following mechanism. At high negative U_{pulse}, oxygen ions are moved from their lattice sites onto interstitial sites [7], forming Frenkel pairs with the remaining V_Os [Fig. 10(c)]. As a consequence of the particles' charge (V_Os in perovskites carry a relative positive charge [50]), the strong electric field $\vec{E}$ results in a separation. V_Os are collected at the surface of the LSMO layer enhancing d_{barrier}, while the O_{is}^{2-} are pushed away from it into the bulk. Additionally, also the barrier height Φ_0 is changed at this point of the RS trace. This is consistent with the assumption that Φ_0 is proportional to the charge density, i.e., the concentration of vacancies c_{V_O}, at the interface.

V_Os can be regarded as rather mobile defects in perovskite oxides [50] which readily explains the minor-loop trace. At intermediate positive U_{pulse}, where $\vec{E}$ is still too weak to significantly move the O_{is}^{2-} ions, V_Os are pushed away from the interface and the device resistance increases [LRS → IRS/HRS; Figs. 10(d) and 10(e)]. Likewise they are attracted to it during the minor-loop transition IRS → LRS (not included in Fig. 10). Hereby both their spatial distribution and c_{V_O} are changed, leading to a modification of both barrier parameters and finally a change in device resistance. The influence of the increasing barrier width is stronger than that of the decreasing barrier height [44] so a broader distribution yields a higher device resistance. When U_{pulse} ($\vec{E}$) reaches a certain magnitude (strength) in the positive regime, the V_O and O_{is}^{2-} distributions are approaching each other. This is because, on the one hand, the O_{is}^{2-} start to move and, on the other hand, d_{barrier} is sufficiently increased. At this point,

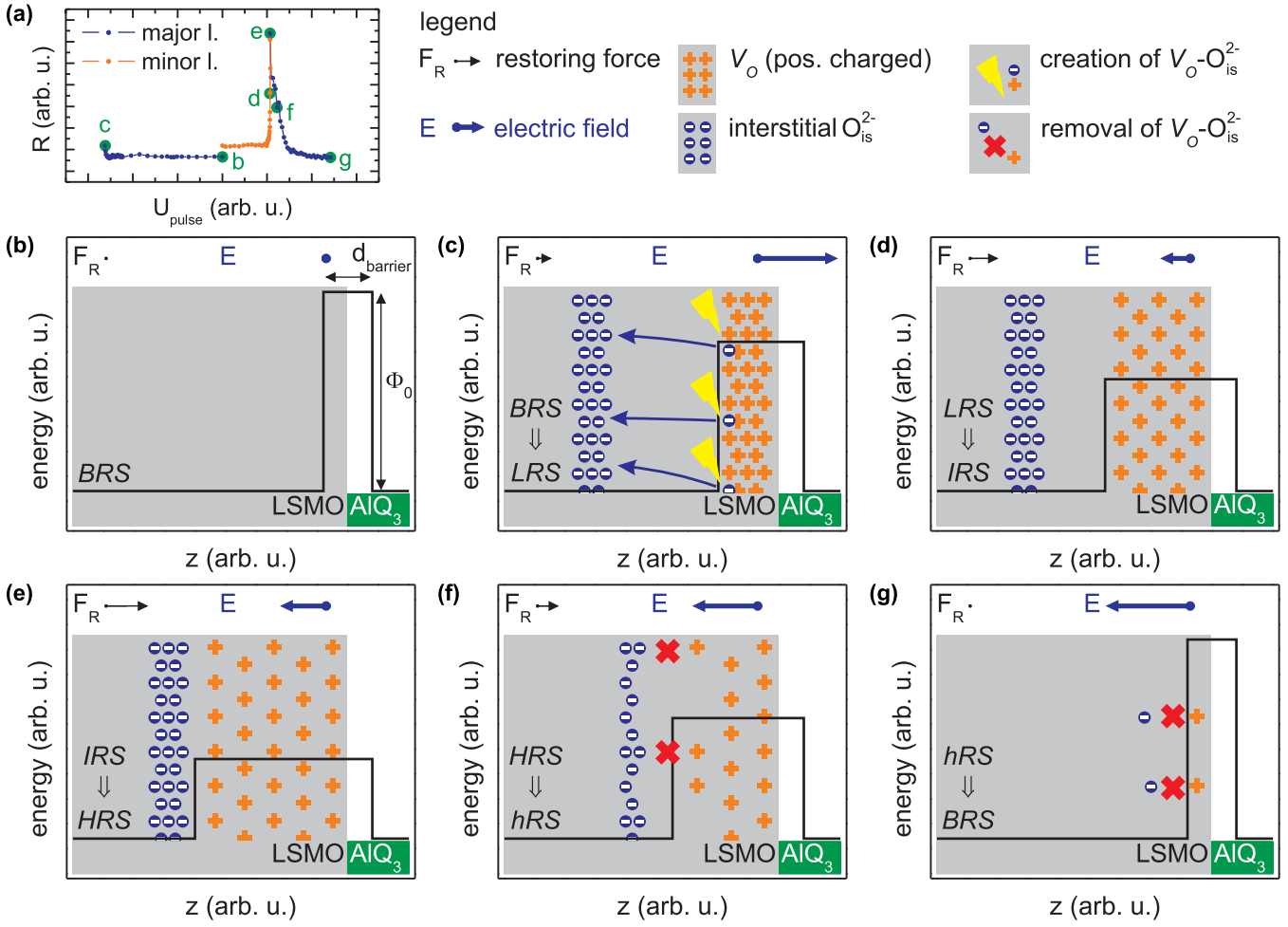

FIG. 10. (Color online) Schematic representation of the proposed model. (a) The model includes the separation of a RS trace into major and minor loop. Distinct points are marked for which the interface LSMO-AlQ_3 is sketched in panels (b)–(g). Arrows in the top of each panel illustrate the strength and direction of the electric field E and the restoring force F_R originating from the lattice distortion that is caused by the change of stoichiometry. Starting from the BRS (b) the initial negative voltage pulse moves O_{is}^{2-} from their lattice site into the LSMO as interstitials, leaving V_Os at the surface (c) which are stabilized by lattice strain. An increasing reverse voltage creates a broadening of the V_Os' distribution while keeping their number constant, causing an increase in barrier width and a decrease in barrier height [(d), (e)]. When the field is high enough V_Os and O_{is}^{2-} recombine (f) and the initial state is restored (g). The intermediate state during the transition HRS → BRS is labeled hRS here.

the aforementioned creation mechanism can be reversed; i.e., effectively V_Os are removed and a decrease of the device resistance is observed in the RS trace [HRS → BRS; Figs. 10(f) and 10(g)].

Furthermore, the results of the heating-cooling procedure for the IRS can be explained by this approach. The introduction of V_Os comes along with a lattice distortion [49] which has a lower energy at the surface. When the V_Os are distributed over a larger volume the distortion creates a higher energy state. This can be taken into account by introducing a restoring force F_R that is proportional to the spatial extension of the V_O distribution [see Figs. 10(b)–10(g)]. At low temperatures, the V_Os' mobility is too low to allow for any significant influence of F_R. At elevated temperatures, however, F_R can drag the V_Os back to the surface due to their thermally enhanced mobility. Obviously and as observed experimentally this only applies for states which depend on the V_O distribution's width, i.e., the IRS and HRS. The LRS and BRS, on the contrary, already represent states with a minimized distortion energy. This reasoning is similar to the one proposed by Nian *et al.* [6] who likewise have observed a temperature-dependent relaxation of resistive states that can be attributed to a strain-enhanced diffusion of defects (V_Os and oxygen ions in $Pr_{0.7}Ca_{0.7}MnO_3$).

B. Application to experimental results

Our phenomenological model does not only yield a qualitative description of the RS effect but likewise can be employed for a quantitative analysis of experimental results. First, it allows for a description of the barrier parameters' dynamics during the minor loops. In the scenario outlined above the increase of the device resistance during the RS minor-loop switching LRS → IRS is due to a motion of V_Os in the applied $\vec{E}$ which changes the V_O distribution and hereby, in the first instance, d_{barrier}. It is now assumed that the V_Os' motion is influenced by $\vec{E}$ only and can be described as a uniformly

accelerated motion with the velocity v_{V_O} and the acceleration a_{V_O}:

$$d_{\text{barrier}} = d_{\text{barrier},0} + v_{V_O} t_{\text{pulse}} = d_{\text{barrier},0} + a_{V_O} t_{\text{pulse}}^2. \quad (1)$$

$d_{\text{barrier},0}$ is the initial barrier thickness (barrier thickness in the LRS). With a V_O's charge q and its mass m the acceleration can be transformed using $a_{V_O} = F/m$ and eventually Eq. (1) can be written as

$$\begin{aligned} d_{\text{barrier}}(U_{\text{single}}) &= d_{\text{barrier},0} + \frac{q|\vec{E}|}{m} t_{\text{pulse}}^2 \\ &= d_{\text{barrier},0} + \frac{q U_{\text{single}}}{d_{\text{barrier}}} \frac{t_{\text{pulse}}^2}{m}. \end{aligned} \quad (2)$$

Equation (2) describes the influence of a single voltage pulse U_{single} on d_{barrier} and can be further simplified by combining all constants to $\alpha = q t_{\text{pulse}}^2/m$. With this, the following solution is obtained for $\Delta d_{\text{barrier}} = d_{\text{barrier}}(U_{\text{single}}) - d_{\text{barrier},0}$:

$$\begin{aligned} &\Delta d_{\text{barrier}}(U_{\text{single}}) \\ &= \frac{-d_{\text{barrier},0} + \sqrt{d_{\text{barrier},0}^2 + 4\alpha U_{\text{single}}}}{2}. \end{aligned} \quad (3)$$

During a measurement a number of pulses is applied to the barrier which leads to a total $\Delta d_{\text{barrier}}$ that can be calculated by integrating $\Delta d_{\text{barrier}}(U_{\text{single}})$. In order to perform this operation, another simplifying assumption has to be made. As can bee seen in all RS traces, during the RS sweep in the positive regime seemingly U_{pulse} needs to overcome a certain threshold U_{th} until a significant change in device resistance appears as transition LRS $\rightarrow$ IRS/HRS. Therefore it is justifiable to replace U_{single} by $U_{\text{pulse}} - U_{th}$. Thus, the integration of Eq. (3) yields

$$\begin{aligned} &\Delta d_{\text{barrier}}(U_{\text{pulse}}) \\ &= \int_0^{U_{\text{pulse}}-U_{th}} \Delta d_{\text{barrier}}(U_{\text{pulse}}) dU_{\text{pulse}} \\ &= \frac{1}{2}\Bigg(-d_{\text{barrier},0}(U_{\text{pulse}} - U_{th}) \\ &\quad + \frac{\left[d_{\text{barrier},0}^2 + 4\alpha(U_{\text{pulse}} - U_{th})\right]^{3/2}}{6\alpha}\Bigg). \end{aligned} \quad (4)$$

The formula displayed in Eq. (4) now can be used to fit the experimental results that are obtained by I/V characterization and Simmons analysis for d_{barrier} during a minor loop [circles in Fig. 11(a)]. $d_{\text{barrier},0}$, U_{th}, and α are the fit parameters, whereby $d_{\text{barrier},0}$ and U_{th} are limited to a certain interval that is determined by the experimentally obtained values.

The best reproductions of the experimental data that can be calculated using Eq. (4) likewise are shown in Fig. 11(a) as line plots for both minor-loop transitions. For the switching IRS $\rightarrow$ LRS, the fit function obviously only has to be modified

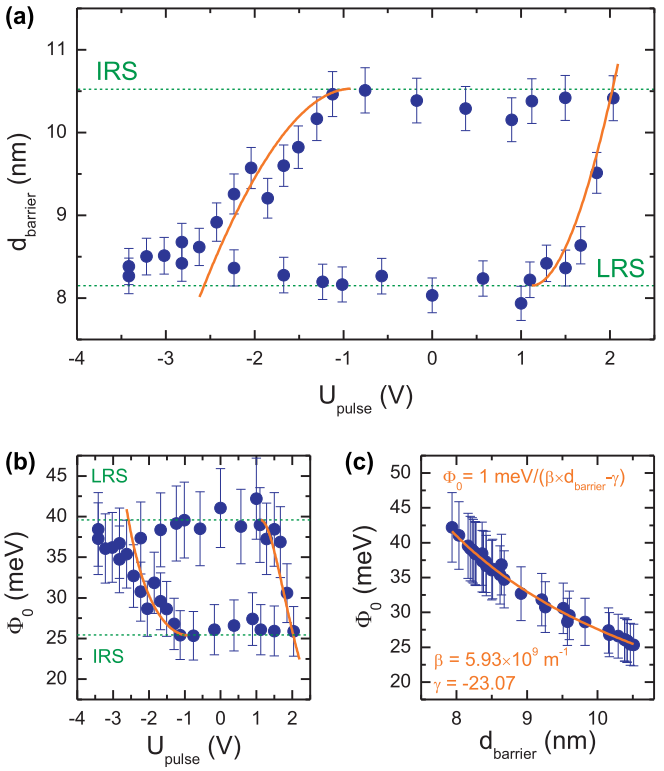

FIG. 11. (Color online) Analysis of a RS minor loop using fitting procedures derived from the proposed model. (a) Change of d_{barrier} during a minor loop determined by Simmons fits [see also Figs. 8(c)–8(e)]. The orange/light gray curves are the results of fits using Eq. (4). (b) Change of Φ_0 during the same minor-loop experiment. The orange/light gray curves here are calculated exploiting the correlation between Φ_0 and d_{barrier} shown in (c). (c) Plotting Φ_0 against d_{barrier} for the minor loop under investigation reveals a clear correlation between the two barrier parameters that can be described by the given expression.

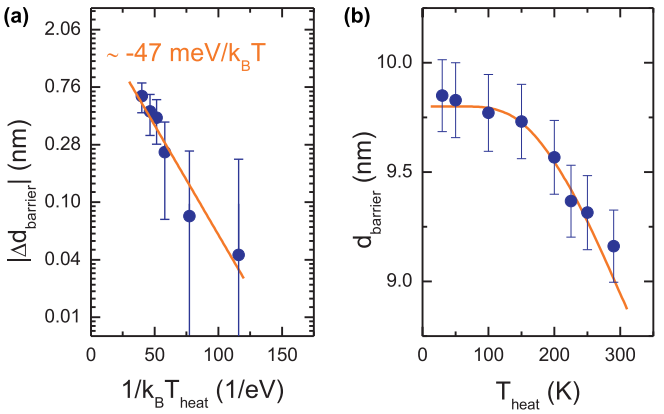

FIG. 12. (Color online) Analysis of heating-cooling cycle experiments using the proposed model. (a) Arrhenius plot of the thermally induced change of d_{barrier} represented as absolute difference of the values determined before and after the heating-cooling cycle. For $T_{\text{heat}} > 100$ K (for the sake of clarity the data for lower T_{heat} are omitted here) a linear fit can be applied to the data (orange/light gray line). The slope of this fit corresponds to the activation energy E_a of the underlying diffusion process. (b) The calculated trace of $d_{\text{barrier}}(T_{\text{heat}})$ matches well the experimentally determined values.

slightly. It can be seen that a good description of the results is provided by the fit for LRS → IRS, while a larger deviation is present for the back-switching process. This is very likely due to the simplifying assumption made above that the V_Os' motion is influenced by $\vec{E}$ only while any other force or field is not taken into account in Eqs. (2) and (3).

Furthermore, the data describing $d_{\mathrm{barrier}}(U_{\mathrm{pulse}})$ can be used to find a fit for $\Phi_0(U_{\mathrm{pulse}})$ as well [Fig. 11(b)]. Evidently experimental and calculated values exhibit a comparable congruence here. The Φ_0 trace is calculated exploiting the fact that there is a clear correlation between d_{barrier} and Φ_0 which is illustrated in Fig. 11(c). It should be mentioned here that this relation agrees rather well with the assumption made in the previous section concerning the dependence of Φ_0 on the V_O concentration, which suggests $\Phi_0 \propto 1/d_{\mathrm{barrier}}$ in the first instance.

Now we turn to the results from the investigations employing heating-cooling cycles, which also can be easily described using the proposed model. As argued above, at elevated temperatures, the restoring force F_R can drag V_Os, which are rather widely distributed when the device is in the IRS, back to the surface due to their enhanced mobility. This relaxation process now is treated as a thermally activated diffusion process the direction of which is determined by F_R. The temperature dependence of the diffusion constant D is given by

$$D(T) = D_0 \exp\left[-\frac{E_a}{k_B T}\right]. \tag{5}$$

E_a is the diffusion process's activation energy. For a further, simplified interpretation the thermally induced change of the barrier width $\Delta d_{\mathrm{barrier}}(T)$ is assumed to be proportional to $D(T)$ (analogously to the Fick's first law):

$$\Delta d_{\mathrm{barrier}}(T_{\mathrm{heat}}) \propto \exp\left[-\frac{E_a}{k_B T_{\mathrm{heat}}}\right]. \tag{6}$$

The relation described by Eq. (6) can be used to fit the experimental results [see Fig. 9(b)] in order to determine E_a. A convenient data representation for this procedure is the so-called Arrhenius plot, i.e., a logarithmic plot over $1/k_B T$. Figure 12(a) contains the Arrhenius plot for $\Delta d_{\mathrm{barrier}}(T_{\mathrm{heat}})$ [taken from Fig. 9(b)]. E_a can be readily extracted from this representation as the slope of a linear fit to the data points. A good fit [line plot in Fig. 12(a)] only is obtained when the data for $T_{\mathrm{heat}} < 100$ K are omitted which for the sake of clarity consequently are not shown here. The activation energy that can be derived from the fit is $E_a = (47 \pm 5)$ meV. In order to obtain an expression describing

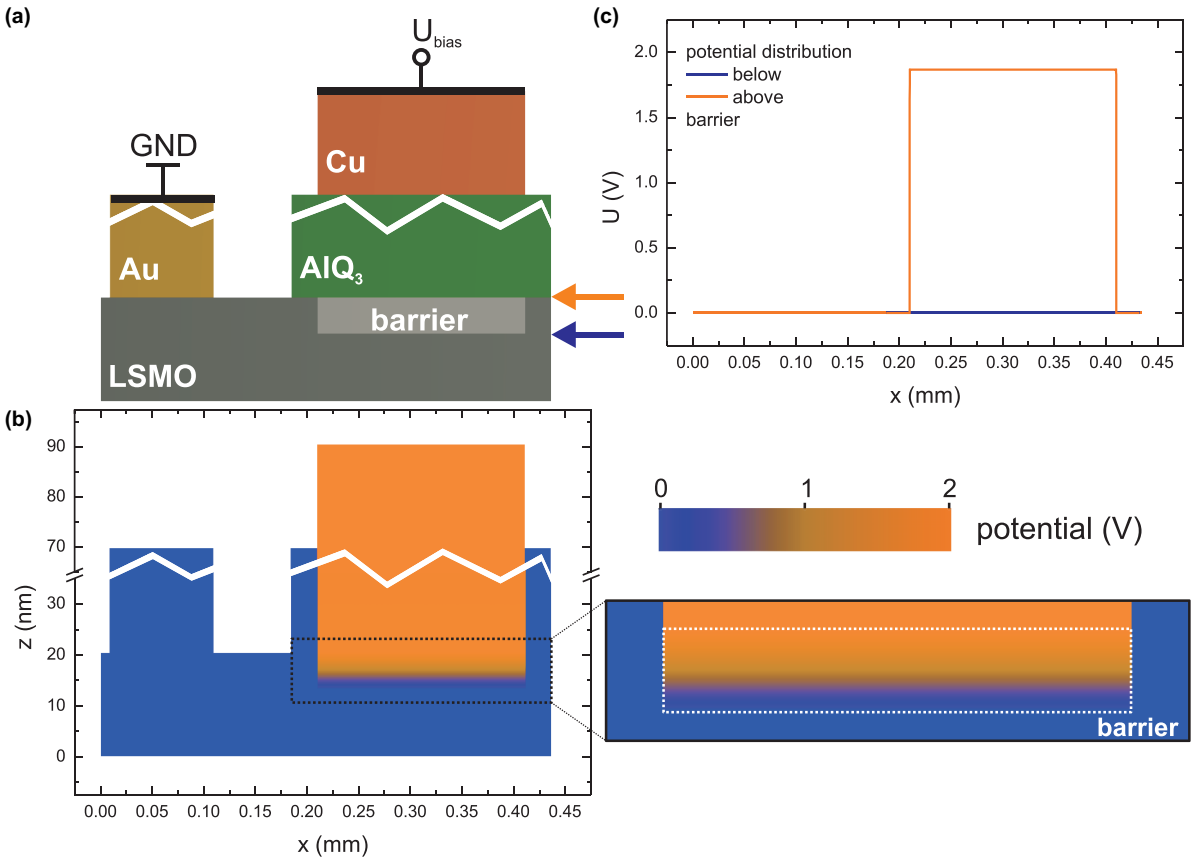

FIG. 13. (Color online) Results of finite element method simulations. (a) Representation of the device layout with $d_{\mathrm{barrier}} = 7$ nm used as input for the simulation. (b) Potential distribution for the complete device calculated for an applied bias of 2 V. The right-hand side shows a blowup of the actual tunnel barrier. For this representation the simulation output has been compressed by a factor of 5000 in the lateral dimension after the simulation for the sake of presentability. (c) Potential distribution below and above the tunnel barrier [see arrows in (a)] represented as line scans.

$d_{\text{barrier}}(T_{\text{heat}})$ we obviously have to subtract the fit function from $d_{\text{barrier}}(4.2\ \text{K})$. Using $E_a = (47 \pm 5)$ meV we finally can compute the trace presented in Fig. 12(b) (line plot) together with the experimental results (circles). Similarly as for the minor-loop results again the calculated data are matching the experimental results quite well.

V. CONCLUSIONS

We have shown results from magnetoresistance measurements and the analysis of RS behavior in organic TAMR devices. The RS is found to be more complex than bipolar switching. In contrast to conventional organic spin-valve devices we can unambiguously identify the observed magnetoresistance effect as TAMR. TAMR successfully has been applied to demonstrate the existence of an injection tunnel barrier at the LSMO-AlQ_3 interface and its modification during RS cycles. The modification of the tunnel barrier has been studied qualitatively and quantitatively by the analysis of I/V characteristics using the Simmons model.

Our findings suggest that the observed RS behavior has its physical origin in the LSMO electrode near its interface to the AlQ_3 layer. We propose a model that is based on the formation, motion, and removal of pairs of oxygen vacancies and interstitial oxygen ions. These mechanisms are initiated by the electric field originating from the voltage pulses. Although final proof for the formation/removal of these defects is still missing, the proposed model provides a complete and qualitatively conclusive picture for all experimental observations. In addition, it also allows for a quantitative analysis of particular features and observations.

Our findings show that RS, which very often is found to be caused in the insulating layer of a metal-insulator-metal structure, can also appear in one of the electrodes of a two-terminal device. In the case of our TAMR structures RS does not only influence the device resistance but also the magnitude of the observed spin-valve signal, which is increased to more than 20%. This interaction can also be exploited in any tunneling device of a similar composition, e.g., conventional organic spin valves with two ferromagnetic electrodes showing a tunneling magnetoresistance [27]. In these devices massive changes of magnetoresistance including sign changes can occur as will be described elsewhere. Thus the results underline the potential of complex oxides to be integrated into multifunctional devices including multistate memory cells or logic.

ACKNOWLEDGMENTS

We thank the EU for funding the research in the project HINTS (Grant No. NMP3-SL-2011-263104) and the DFG for financial support in the SFB762. The authors also gratefully acknowledge fruitful discussions with M. Bron and S. Ebbinghaus.

APPENDIX A: FINITE ELEMENT METHOD SIMULATIONS

Numerical simulations using Elmer [51] have been performed in order to verify the tunnel barrier's homogeneity which is a crucial prerequisite for the applicability of any I/V curve analysis. For the simulations the two-dimensional representation of the device shown in Fig. 13(a) has been chosen. The structure and the simulation output displayed in Figs. 13(a) and 13(b) are compressed in the lateral dimension in order to ensure presentability. During the actual simulation realistic dimensions have been used and the simulation output in Fig. 13(b) has been scaled after the calculation only. The view of the device corresponds to Fig. 1(c).

As can be seen from Fig. 13(b) which comprises simulation results for $d_{\text{barrier}} = 7$ nm, the potential distribution in the lateral direction is constant for every z in the actual device area. Thus, the surfaces below and above the tunnel barrier are equipotential planes and consequently the tunneling current density can be considered homogeneous over the barrier. This becomes even more evident regarding the line scans in Fig. 13(c) that are extracted from the data in Fig. 13(b).

APPENDIX B: I/V CURVE ANALYSIS: SIMMONS MODEL

Several models have been established for the analysis of tunnel barriers based on suitable fitting procedures applied to I/V curves. For the rather simple case of a symmetric rectangular tunnel barrier (thickness d_{barrier}, height Φ_0) the model proposed by Simmons [44] provides a good theoretical description.

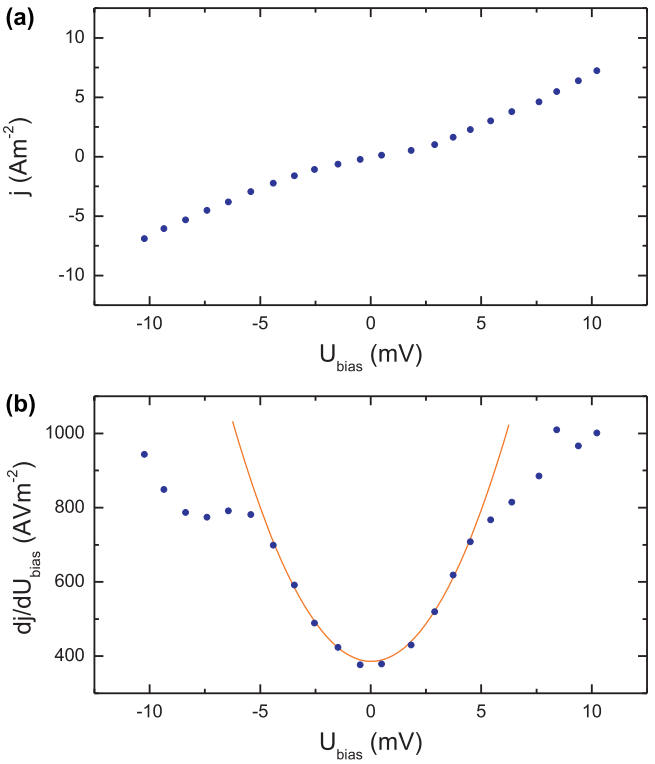

FIG. 14. (Color online) Typical I/V analysis using the Simmons model. (a) Results of I/V characterization represented as current density j plotted against the bias voltage U_{bias}. (b) Calculated differential conductance (points) and quadratic fit according to the Simmons model (line).

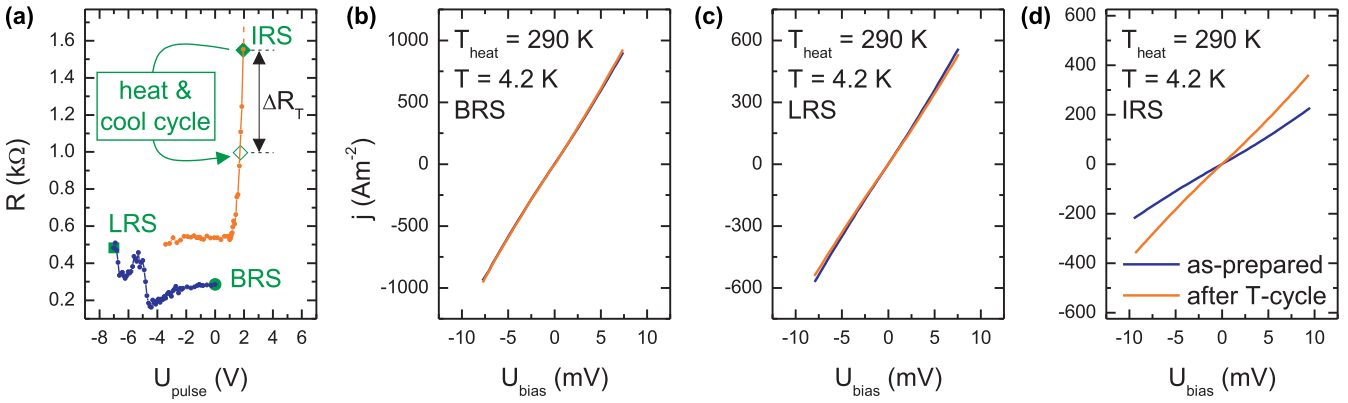

FIG. 15. (Color online) I/V curves taken before and after heating-cooling cycles. (a) RS trace comprising the three distinguished states under investigation. (b)–(d) I/V responses are recorded before (blue/dark gray curves) and after (orange/light gray curves) an interim temperature change from 4.2 K to 290 K and back. The results reveal different stabilities of the states upon the temperature increase.

In this model the tunnel current density j at an applied voltage U_{bias} is described as follows:

$$j = \frac{e}{4\pi^2\hbar d_{\text{barrier}}^2}\left\{\left(\Phi_0 - \frac{eU_{\text{bias}}}{2}\right)\times \exp\left[-\frac{\sqrt{8m}}{\hbar}\left(\Phi_0 - \frac{eU_{\text{bias}}}{2}\right)^{1/2} d_{\text{barrier}}\right] - \left(\Phi_0 + \frac{eU_{\text{bias}}}{2}\right)\times \exp\left[-\frac{\sqrt{8m}}{\hbar}\left(\Phi_0 + \frac{eU_{\text{bias}}}{2}\right)^{1/2} d_{\text{barrier}}\right]\right\}. \quad \text{(B1)}$$

m is the electron rest mass, $\hbar$ the reduced Planck constant, and e the elementary charge. j in Eq. (B1) is derived from more general formulas assuming $eU_{\text{bias}} < \Phi_0$ (bias voltage small compared to the barrier height). The differential tunnel conductance $G = dj/dU_{\text{bias}}$ can be calculated from Eq. (B1):

$$G(U) = G(0) + G(0)\left(\frac{e^2 m}{4\hbar^2}\frac{d_{\text{barrier}}^2}{\Phi_0}\right)U_{\text{bias}}^2 \quad \text{(B2)}$$

with

$$G(0) = \frac{e^2}{4\pi^2\hbar^2 d_{\text{barrier}}}\sqrt{2m\Phi_0}\exp\left(-\frac{\sqrt{8m}}{\hbar}\sqrt{\Phi_0}d_{\text{barrier}}\right). \quad \text{(B3)}$$

As can be seen from Eqs. (B2) and (B3) G, and hereby equally a device's resistance $R \propto 1/G$, is mainly governed by d_{barrier}. Furthermore, using Eqs. (B2) and (B3) the barrier parameters Φ_0 and d_{barrier} can be determined from a quadratic fit to $G(U_{\text{bias}})$. Figure 14(a) shows one of the numerous I/V characteristics analyzed within the framework of the presented investigations and Fig. 14(b) the respective differential conductance including the Simmons fit. The data in Fig. 14(b) reveal a significant deviation from the quadratic behavior for $|U_{\text{bias}}| \gtrsim 5$ mV. Therefore, the data input for the fitting process is limited to $|U_{\text{bias}}| < 5$ mV for all I/V analysis performed in the scope of this work. For the barrier parameters values of $\Phi_0 = (17.2 \pm 2.4)$ meV and $d_{\text{barrier}} = (15.2 \pm 0.5)$ nm can be determined from the fit in Fig. 14(b) evaluating Eqs. (B2) and (B3).

APPENDIX C: HEATING-COOLING CYCLES: I/V CURVES

In Fig. 15 the preliminary study concerning the stability of the resistive states upon an interim increase of the temperature is summarized. Figure 15(a) shows the result of the RS measurement that is used for the preparation of the three states under investigation (BRS, LRS, and one IRS with $\Delta R_{\text{ML}} \approx 1$ kΩ).

Two I/V curves are recorded for each state, one before (blue/dark gray curves) and one after (orange/light gray curves) the respective heating-cooling cycle [Figs. 15(b)–15(d)]. As stated in the main text, both I/V curves coincide in the case of the BRS and LRS; i.e., those states are not influenced by the temperature change. A significant modification, however, is obtained for the IRS, namely a decrease of the device resistance. A reduction of ΔR_{ML} by ∼55% can be calculated from the I/V traces, which is also illustrated by the green/gray arrow in Fig. 15(a).

[1] T. W. Hickmott, J. Appl. Phys. **33**, 2669 (1962).
[2] L. O. Chua, IEEE Trans. Circuit Theory **18**, 507 (1971).
[3] W. R. Hiatt and T. W. Hickmott, Appl. Phys. Lett. **6**, 106 (1965).
[4] A. Baikalov, Y. Q. Wang, B. Shen, B. Lorenz, S. Tsui, Y. Y. Sun, Y. Y. Xue, and C. W. Chu, Appl. Phys. Lett. **83**, 957 (2003).
[5] S. Tsui, A. Baikalov, J. Cmaidalka, Y. Y. Sun, Y. Q. Wang, Y. Y. Xue, C. W. Chu, L. Chen, and A. J. Jacobson, Appl. Phys. Lett. **85**, 317 (2004).
[6] Y. B. Nian, J. Strozier, N. J. Wu, X. Chen, and A. Ignatiev, Phys. Rev. Lett. **98**, 146403 (2007).
[7] R. Dong, W. F. Xiang, D. S. Lee, S. J. Oh, D. J. Seong, S. H. Heo, H. J. Choi, M. J. Kwon, M. Chang, M. Jo, M. Hasan, and H. Hwang, Appl. Phys. Lett. **90**, 182118 (2007).
[8] R. Waser and M. Aono, Nat. Mater. **6**, 833 (2007).
[9] A. Sawa, Mater. Today **11**, 28 (2008).

[10] M. K. Yang, J.-W. Park, T. K. Ko, and J.-K. Lee, Appl. Phys. Lett. **95**, 042105 (2009).
[11] D.-H. Kwon, K. M. Kim, J. H. Jang, J. M. Jeon, M. H. Lee, G. H. Kim, X. S. Li, G.-S. Park, B. Lee, S. Han, M. Kim, and C. S. Hwang, Nat. Nanotechnol. **5**, 148 (2010).
[12] C. Moreno, C. Munuera, S. Valencia, F. Kronast, X. Obradors, and C. Ocal, Nano Lett. **10**, 3828 (2010).
[13] T. Baiatu, R. Waser, and K.-H. Härdtl, J. Am. Ceram. Soc. **73**, 1663 (1990).
[14] M. J. Rozenberg, I. H. Inoue, and M. J. Sánchez, Phys. Rev. Lett. **92**, 178302 (2004).
[15] J. Jeong, N. Aetukuri, T. Graf, T. D. Schladt, M. G. Samant, and S. S. P. Parkin, Science **339**, 1402 (2013).
[16] L. P. Ma, J. Liu, and Y. Yang, Appl. Phys. Lett. **80**, 2997 (2002).
[17] J. Y. Ouyang, C. W. Chu, C. R. Szmanda, L. P. Ma, and Y. Yang, Nat. Mater. **3**, 918 (2004).
[18] J. H. A. Smits, S. C. J. Meskers, R. A. J. Janssen, A. W. Marsman, and D. M. de Leeuw, Adv. Mater. **17**, 1169 (2005).
[19] A. K. Mahapatro, R. Agrawal, and S. Ghosh, J. Appl. Phys. **96**, 3583 (2004).
[20] L. E. Hueso, I. Bergenti, A. Riminucci, Y. Q. Zhan, and V. A. Dediu, Adv. Mater. **19**, 2639 (2007).
[21] P.-T. Lee, T.-Y. Chang, and S.-Y. Chen, Org. Electron. **9**, 916 (2008).
[22] T.-Y. Chang, Y.-W. Cheng, and P.-T. Lee, Appl. Phys. Lett. **96**, 043309 (2010).
[23] M. Prezioso, A. Riminucci, I. Bergenti, P. Graziosi, D. Brunel, and V. A. Dediu, Adv. Mater. **23**, 1371 (2011).
[24] B. Cho, S. Song, Y. Ji, T.-W. Kim, and T. Lee, Adv. Funct. Mater. **21**, 2806 (2011).
[25] M. Prezioso, A. Riminucci, P. Graziosi, I. Bergenti, R. Rakshit, R. Cecchini, A. Vianelli, F. Borgatti, N. Haag, M. Willis, A. J. Drew, W. P. Gillin, and V. A. Dediu, Adv. Mater. **25**, 534 (2012).
[26] A. Riminucci, M. Prezioso, C. Pernechele, P. Graziosi, I. Bergenti, R. Cecchini, M. Calbucci, M. Solzi, and V. A. Dediu, Appl. Phys. Lett. **102**, 092407 (2013).
[27] M. Grünewald, R. Göckeritz, N. Homonnay, F. Würthner, L. W. Molenkamp, and G. Schmidt, Phys. Rev. B **88**, 085319 (2013).
[28] I. D. Parker, J. Appl. Phys. **75**, 1656 (1994).
[29] M. A. Baldo and S. R. Forrest, Phys. Rev. B **64**, 085201 (2001).
[30] C. Gould, C. Rüster, T. Jungwirth, E. Girgis, G. M. Schott, R. Giraud, K. Brunner, G. Schmidt, and L. W. Molenkamp, Phys. Rev. Lett. **93**, 117203 (2004).
[31] K. I. Bolotin, F. Kuemmeth, and D. C. Ralph, Phys. Rev. Lett. **97**, 127202 (2006).
[32] J. Moser, A. Matos-Abiague, D. Schuh, W. Wegscheider, J. Fabian, and D. Weiss, Phys. Rev. Lett. **99**, 056601 (2007).
[33] B. G. Park, J. Wunderlich, D. A. Williams, S. J. Joo, K. Y. Jung, K. H. Shin, K. Olejník, A. B. Shick, and T. Jungwirth, Phys. Rev. Lett. **100**, 087204 (2008).
[34] M. Grünewald, M. Wahler, F. Schumann, M. Michelfeit, C. Gould, R. Schmidt, F. Würthner, G. Schmidt, and L. W. Molenkamp, Phys. Rev. B **84**, 125208 (2011).
[35] Z. H. Xiong, D. Wu, Z. V. Vardeny, and J. Shi, Nature (London) **427**, 821 (2004).
[36] T. S. Santos, J. S. Lee, P. Migdal, I. C. Lekshmi, B. Satpati, and J. S. Moodera, Phys. Rev. Lett. **98**, 016601 (2007).
[37] H. Vinzelberg, J. Schumann, D. Elefant, R. B. Gangineni, J. Thomas, and B. Büchner, J. Appl. Phys. **103**, 093720 (2008).
[38] A. J. Drew, J. Hoppler, L. Schulz, F. L. Pratt, P. Desai, P. Shakya, T. Kreouzis, W. P. Gillin, A. Suter, N. A. Morley, V. K. Malik, A. Dubroka, K. W. Kim, H. Bouyanfif, F. Bourqui, C. Bernhard, R. Scheuermann, G. J. Nieuwenhuys, T. Prokscha, and E. Morenzoni, Nat. Mater. **8**, 109 (2009).
[39] J. Rybicki, R. Lin, F. Wang, M. Wohlgenannt, C. He, T. Sanders, and Y. Suzuki, Phys. Rev. Lett. **109**, 076603 (2012).
[40] M. Mathews, F. M. Postma, J. C. Lodder, R. Jansen, G. Rijnders, and D. H. A. Blank, Appl. Phys. Lett. **87**, 242507 (2005).
[41] R. P. Cowburn, S. J. Gray, J. Ferré, J. A. C. Bland, and J. Miltat, J. Appl. Phys. **78**, 7210 (1995).
[42] Y. Zhan and M. Fahlman, J. Polym. Sci., Part B: Polym. Phys. **50**, 1453 (2012).
[43] Y. Zahn, I. Bergenti, L. E. Hueso, V. Dediu, M. P. de Jong, and Z. S. Li, Phys. Rev. B **76**, 045406 (2007).
[44] J. G. Simmons, J. Appl. Phys. **34**, 1793 (1963).
[45] R. H. Fowler and L. Nordheim, Proc. R. Soc. A **119**, 173 (1928).
[46] A. Goyal, M. Rajeswari, R. Shreekala, S. E. Lofland, S. M. Bhagat, T. Boettcher, C. Kwon, R. Ramesh, and T. Venkatesan, Appl. Phys. Lett. **71**, 2535 (1997).
[47] M. Rajeswari, R. Shreekala, A. Goyal, S. E. Lofland, S. M. Bhagat, K. Ghosh, R. P. Sharma, R. L. Greene, R. Ramesh, T. Venkatesan, and T. Boettcher, Appl. Phys. Lett. **73**, 2672 (1998).
[48] J. Dho, N. H. Hur, I. S. Kim, and Y. K. Park, J. Appl. Phys. **94**, 7670 (2003).
[49] T. Li, B. Wang, H. H. Dai, Y. S. Du, H. Yan, and Y. P. Liu, J. Appl. Phys. **98**, 123505 (2005).
[50] R. Waser, T. Baiatu, and K.-H. Härdtl, J. Am. Ceram. Soc. **73**, 1654 (1990).
[51] See http://www.csc.fi/english/pages/elmer